Journal of Solid State Chemistry 305 (2022) 122696

Contents lists available at ScienceDirect

Journal of Solid State Chemistry

journal homepage: www.elsevier.com/locate/jssc

Effect of spark plasma sintering temperature on microstructure and thermoelectric properties of the cermet composites consisting of $Bi_2Te_{2.1}Se_{0.9}$ matrix and $Co@CoTe_2$ inclusions

Marina Zhezhu [a], Alexei Vasil'ev [b], Maxim Yaprintsev [a], Oleg Ivanov [b,*], Vseslav Novikov [a,b]

[a] Belgorod State University, Belgorod 308015, Russia
[b] Belgorod State Technological University Named After V.G. Shukhov, Belgorod 308012, Russia

ARTICLE INFO

Keywords:
Cermet
Spark-plasma sintering
Texturing
"core"-"shell" inclusions
Thermoelectric properties

ABSTRACT

Novel cermet $Bi_2Te_{2.1}Se_{0.9}$+0.33 wt% Co composite has been prepared via spark plasma sintering (SPS) the starting $Bi_2Te_{2.1}Se_{0.9}$ and Co powders at different SPS-temperatures (T_S = 598, 623, 648 and 673 K). During the sintering, initial Co inclusions transform into final filler $Co@CoTe_2$ ("core"-"shell") inclusions, randomly distributed inside textured grained $Bi_2Te_{2.1}Se_{0.9}$ matrix. Forming these inclusions is originated from high-temperature chemical interaction between $Bi_2Te_{2.1}Se_{0.9}$ and Co. Main features in microstructure and thermoelectric properties of the cermet composite found with increasing T_S are: (i) a texturing degree of grained $Bi_2Te_{2.1}Se_{0.9}$ matrix gradually decreases that is attributed to reducing in ability of initial nanometer Co particles to act as lubricant; (ii) a fraction of the Co core decreases, and a fraction of the $CoTe_2$ shell increases that is related to acceleration of $Co \rightarrow CoTe_2$ reaction at higher temperatures; (iii) the specific electrical resistivity and the Seebeck coefficient reduce, whereas the total thermal conductivity increases that can be originated from growth of electron concentration due to local Co doping. Highest value of the thermoelectric figure-of-merit equal to ~0.8 was observed for the composite, SPS-treated at 673 K.

1. Introduction

Generally, any composite consists of two, at least, individual components, which are remarkably differing in their physical and/or chemical properties [1–3]. Main microstructural elements of a composite are matrix and filler. Usually, embedding filler into a matrix allows improving desired properties of the matrix material. It is important to note that these properties of the composite itself are often superior to those of its individual components. Moreover, some novel properties, which are not characteristic for the individual components, can be also appeared in the composite. Specific properties of various types' composites are controlled by properties of matrix and filler materials, and size, shape, dimension and content of filler, distributed inside matrix. Currently, cermet composites (or cermets) consisting of ceramic matrix (Al_2O_3, ZrO_2, SiC, etc.) and metal filler (Cr, Ti, Al, Mo, etc) are important type of composites, attractive for practice [4–6]. Embedding metal filler results in increasing the strength wear and heat resistance, and improving the anticorrosive properties of cermet composites. Therefore, the cermets should be primarily considered as structural materials that can be widely applied in aircraft construction, automotive, mechanical engineering, etc. Sometimes, the cermets are also developed to improve the functional (mainly electrical or magnetic) properties [7]. In particular, one of promising approaches of modern thermoelectric materials science is based on developing thermoelectric magnetic cermets, consisting of common thermoelectric taken as a ceramic matrix, and a metal filler possessing ferromagnetic properties (transient *d*-metals) [8–12]. In the thermoelectric magnetic cermets, specific physical mechanisms can be simultaneously affected their main thermoelectric properties (the specific electrical resistivity, ρ, the Seebeck coefficient, S, and the total thermal conductivity, k). In accordance with Refs. [8–12], the main mechanisms can be listed as follows: (a) scattering electrons and phonons by metal inclusions, affecting ρ and k, respectively; (b) increasing S via an electron energy filtration effect, related to matrix/filler interfaces; (c) scattering electrons by magnetic moments of metal inclusions (similarly to the Kondo effect), resulting in decreasing electron mobility; (d) increasing electron concentration due to rectifying properties of metal-semiconductor contact, which is related to matrix/filler interface, affecting ρ; (e) localizing electrons near matrix/filler interface, resulting

* Corresponding author.
E-mail address: Ivanov.Oleg@bsu.edu.ru (O. Ivanov).

https://doi.org/10.1016/j.jssc.2021.122696
Received 30 August 2021; Received in revised form 21 October 2021; Accepted 26 October 2021
Available online 29 October 2021

in relevant decreasing their mobility and forming magnetic polarons; (f) entrainment effect of carriers by paramagnons (paramagnon drag), affecting ρ, S and k. Similarly to other common composites, the thermoelectric properties of the thermoelectric magnetic cermets will be remarkably dependent on features of their microstructure, including average size of grains in matrix material, type and degree of grains ordering, size, shape and internal structure of filler inclusions and etc. To get a desired microstructure of the cermet with controlled features listed above, some technological variables applying to fabricate the cermet should be correctly tuned. Sintering temperature is one of such easily changeable and controlled variables.

The purpose of this paper is to prepare novel thermoelectric magnetic cermet, consisting of grained $Bi_2Te_{2.1}Se_{0.9}$ matrix and metal ferromagnetic Co filler, and to find and analyze the patterns of spark plasma sintering (SPS) temperature effect on features in the microstructure and thermoelectric properties of this cermet. The Bi_2Te_3-based semiconductors are widely applied to prepare two-component n-type $Bi_2Te_{3-x}Se_x$ and p-type $Bi_{2-x}Sb_xTe_3$ alloys for various low-temperature thermoelectric applications [13,14]. The filler Co metal is ferromagnet with the Curie temperature at 1394 K [15]. It is important to note that the SPS method allows preparing textured samples of Bi_2Te_3-based alloys with a preferential orientation of grains [16–22]. Under the texturing, anisotropy in the thermoelectric properties of the grained material, which is inherent to single crystal, is partially recovering. As result, the properties measured along directions, which are parallel or perpendicular to a texturing axis, are remarkably different, that allows using the texturing to enhance the thermoelectric figure-of-merit of thermoelectric materials. According to Ref. [23], anisotropy in the thermoelectric properties of $Bi_2Te_{3-x}Se_x$ alloys (with $0.3 \leq x \leq 0.9$) was dependent on Se content. The highest anisotropy was observed for composition with $x = 0.9$. Therefore, under spark plasma sintering the cermet composite with grained $Bi_2Te_{2.1}Se_{0.9}$ matrix, anisotropy in the thermoelectric properties resulting from the texturing is expected to be maximal.

2. Materials and methods

To prepare the cermet $Bi_2Te_{2.1}Se_{0.9}$+0.33 wt% Co composite, starting $Bi_2Te_{2.1}Se_{0.9}$ and Co powders were first synthesized. To synthesize the starting $Bi_2Te_{2.1}Se_{0.9}$ powder, the polyol method was applied. The high pure Bi_2O_3, $NaHSeO_3$, TeO_2 precursors taken in a stoichiometric ratio were dissolved in ethylene glycol with 200 g addition of alkaline agent (KOH). The obtained solution was transferred to a 3000 ml round-bottom flask and heated to boiling point at 458 K. After evaporation of water impurity, the flask with solution was then sealed with a reflux and maintained for 4 h at 458 K. The resulted dark suspension was cooled to room temperature. The powder was purified by centrifugation and washing for 3 times with ethanol and acetone. Then, the powder was dried in vacuum drying oven at 373 K for 12 h. To synthesize the starting Co powder, 10 g $Co(NO_3)_2{\cdot}6H_2O$ and 15 g citric acid taken as a coordinating agent were dissolved in 400 ml ethylene glycol. Subsequently, 10 g KOH was added into the solution. The mixture was heated to 353 K under vigorously stirring to homogeneity. Then the resulted solution was cooled to room temperature. Hydrazine hydrate 10 ml was slowly added follow. The reaction mixture heated to 353 K and maintained to 6 h to complete the reduction $Co^{2+} \rightarrow Co^0$ process. The obtained powder was collected by neodymium magnet and washed with ethanol and acetone to remove organic impurities. To prepare the bulk cermet $Bi_2Te_{2.1}Se_{0.9}$+0.33 wt% Co composite, the starting Bi_2Te_3 and Co powders taken in a stoichiometric ratio were thoroughly mixed by a planetary mill for 30 min. The mixed powders were SPS-treated at pressure of 40 MPa for 5 min, resulting in the Ø20 mm × 15 mm cylinders. Different SPS temperatures, T_S, equal to 598, 623, 648 and 673 K were used. To study the thermoelectric properties, the 2 × 2 × 10 mm bars and the Ø10 × 2 mm disks were cut out both along in-plane and out-of-plane directions of the cylinders.

To measure density of the samples SPS-prepared at different temperatures, the Archimedes method was applied. To identify crystal structure and phase composition of the starting $Bi_2Te_{2.1}Se_{0.9}$ and Co powders and the bulk samples, X-ray diffraction (XRD) analysis was performed by using a Rigaku Ultima IV diffractometer with CuK_α-radiation. The Rietveld refinement was applied to calculate crystal lattice parameters for various phases, observed in the starting powders and the bulk samples. To examine morphology of the starting $Bi_2Te_{2.1}Se_{0.9}$ and Co powders, a scanning electron microscope (SEM) Nova NanoSEM 450JEM-2100 was used. This microscope was also applied to find features in microstructure of the bulk samples, related to grain structure and filler inclusions structure, distinguish different phases related to filler inclusions (by backscattered electron (BSE) method) and take profiles of elements along line crossing inclusions (by energy dispersive X-ray spectroscopy (EDS) method). To measure the specific electrical resistivity and the Seebeck coefficient of the bar samples, a ZEM-3 system was used. To determine the total thermal conductivity of the disk-shaped samples, a TC-1200 system using a laser flash method was applied.

3. Results and discussion

According to XRD analysis, the starting $Bi_2Te_{2.1}Se_{0.9}$ powder is single hexagonal $R\bar{3}m$ phase with lattice $a = b = 0.4304$ nm and $c = 3.0000$ nm parameters. Particles in the powder are mainly hexagonal plates with average plate size of a few hundreds of nm and width of ~100 nm (SEM image in Fig. 1 (a). The hexagonal plates are often forming during chemical synthesis of powders of Bi_2Te_3-based compounds [24–27]. The hexagonal habitus of the particles in the powders is directly due to specific features in the crystal layered structure and the chemical mixed between covalent and Van-der-Waals bonding that are specific for these compounds [28,29]. The starting Co powder is single hexagonal $P6_3/mmc$ phase with $a = 0.2507$ nm and $c = 0.4069$ nm parameters. As is shown in SEM image (Fig. 1 (b)), the powder mainly consists of agglomerated formations, having almost spherical shape with the diameter of 3–4 μm.

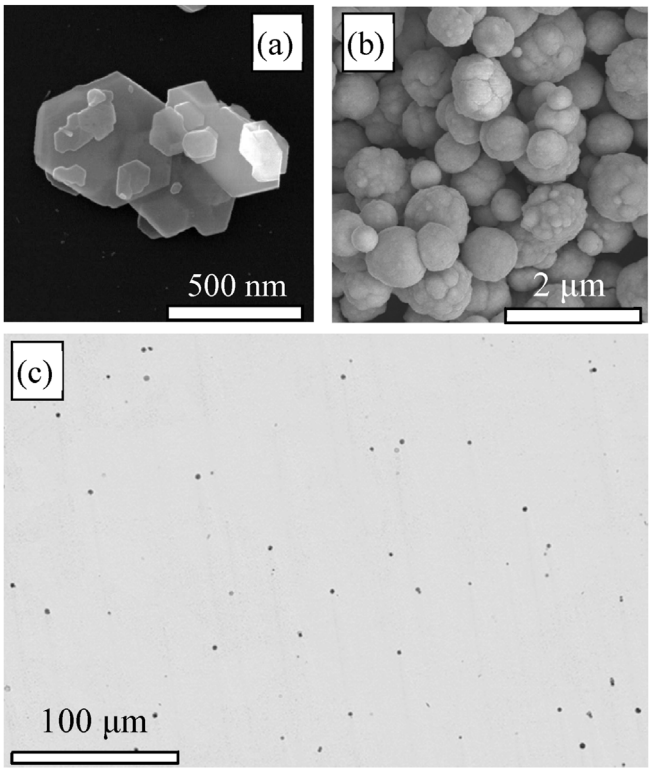

Fig. 1. (a) SEM image of particles in the starting $Bi_2Te_{2.1}Se_{0.9}$ powder; (b) SEM image of agglomerated formations in the starting Co powder; (c) BSE image of polished surface of the cermet $Bi_2Te_{2.1}Se_{0.9}$+0.33 wt% Co composite, SPS-treated at $T_S = 598$ K.

Since the Curie temperature for Co is much higher than room temperature (1394 K), agglomerating separated Co particles can be resulted from a ferromagnetic interaction between the particles [15]. Size of the separate Co particles was estimated as one hundred of nm. Forming a desired matrix-filler microstructure in the cermet $Bi_2Te_{2.1}Se_{0.9}$+0.33 wt % Co composite is proven by BSE image (Fig. 1 (c)). This image taken from polished surface of the composite, SPS-treated at T_S = 573 K. Actually, the filler inclusions, which are randomly distributed inside the matrix, can be observed in this image. Therefore, under SPS-treatment, the starting $Bi_2Te_{2.1}Se_{0.9}$ and Co powders are really transforming into the matrix-filler microstructure. Density of all the samples SPS-prepared at various temperatures was found to be very weakly and irregularly T_S dependent and approximately equal to 7.62 g/cm^3. This value is in good agreement with data published in Ref. [23].

Overall XRD pattern taken for the cermet $Bi_2Te_{2.1}Se_{0.9}$+0.33 wt% Co composite is expected to be simple superposition of XRD patterns, corresponding to the $Bi_2Te_{2.1}Se_{0.9}$ matrix and the Co filler. Owing to large content of the matrix material, its contribution into the overall XRD pattern is dominant, as is shown for the composite, SPS-treated at T_S = 673 K (Fig. 2 (a)). This XRD contribution for the composites sintered at different T_S corresponds to the crystal$R\bar{3}m$ structure, like the starting $Bi_2Te_{2.1}Se_{0.9}$ powder. Therefore, the crystal symmetry of the matrix material does not change with varying T_S. In turn, owing to extremely small content of the filler, its contribution to the overall XRD pattern cannot be reliable distinguished, since intensities of reflections peaks for the filler phase are comparable with background change in the overall XRD pattern. However, as will be shown below, the Co phase really is in filler inclusions of the cermet $Bi_2Te_{2.1}Se_{0.9}$+0.33 wt % Co composite. It is important to note that a new $CoTe_2$ phase is forming in the composite during SPS-treatment of the starting $Bi_2Te_{2.1}Se_{0.9}$ and Co powders. The new phase has orthorhombic *Pnam* structure with lattice a = 0.5217, b = 0.6220 and c = 0.5426 nm parameters. The most of peaks, which correspond to the $Bi_2Te_{2.1}Se_{0.9}$ and $CoTe_2$ phases, are partially or totally overlapped. However, some of separate peaks for the $CoTe_2$ phases can be yet observed. Enlarged part of the overall XRD patterns, which shows forming the $CoTe_2$ phase in the composites SPS-treated at T_S = 598 and 673 K is presented in Fig. 2 (b). Additional weak (230) peak, which is characteristic of the $CoTe_2$ phase, is appearing at left slope of main (015) peak of the $Bi_2Te_{2.1}Se_{0.9}$ phase. A fraction of the $CoTe_2$ phase is apparently increasing with growing T_S, since the (230) peak for the composite with T_S = 673 K (curve *2*) is much higher as compared to that for the composite with T_S = 598 K (*1*).

Coexistence of the $Bi_2Te_{2.1}Se_{0.9}$, Co and $CoTe_2$ phases in the cermet $Bi_2Te_{2.1}Se_{0.9}$+0.33 wt % Co composite can be confirmed by analysis of BSE image and mapping of elements distribution per surface of the cermet composite. BSE image of polished surface, with which different elements were mapped, is shown in Fig. 3 (a). Three different phases can be found in this Figure. Major phase corresponds to a light-grayed background, while minor phases are filler inclusions, which are randomly distributed inside the major phase. The filler inclusions themselves are composite ones, since they are formed as "core"-"shell" inclusions. According to Bi, Te, Se and Co maps (Fig. 3 (b), (c), (d), (e) and (f)), major phase should be attributed to the matrix $Bi_2Te_{2.1}Se_{0.9}$ phase, whereas minor Co and $CoTe_2$ phases form the filler inclusions. These slightly distorted spherical inclusions consist of a Co core covered with a $CoTe_2$ shell, i.e. Co@$CoTe_2$ inclusions are naturally formed in the cermet composite during SPS-process. Recently, forming similar filler Ni@$NiTe_2$ inclusions called as locally-gradient domains was also found in the Bi_2Te_3-matrix + Ni-filler composite [11,12].

To characterize a distribution of different elements inside the "core"-"shell" inclusions, which form in the cermet $Bi_2Te_{2.1}Se_{0.9}$+0.33 wt% Co

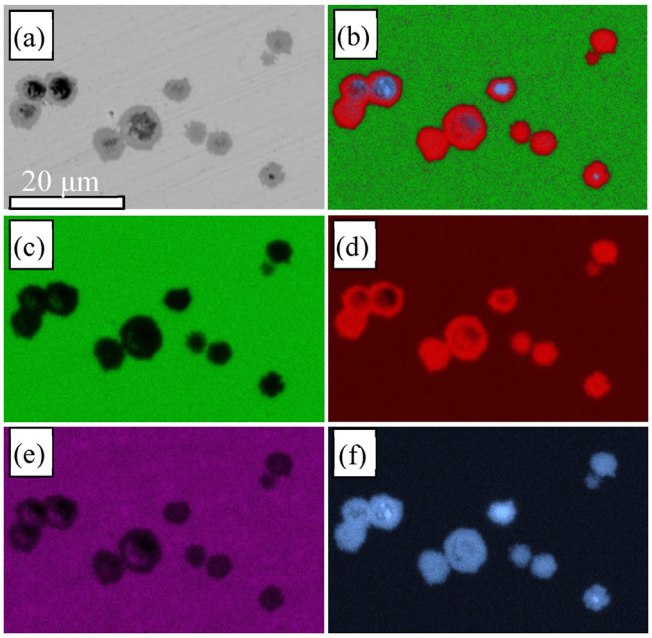

Fig. 3. BSE image of polished surface (a), distribution map of all Bi, Te, Se and Co elements (b) and distribution maps of individual Bi (c), Te (d), Se (d) and Co (f) for the cermet $Bi_2Te_{2.1}Se_{0.9}$+0.33 wt% Co composite, SPS-treated at T_S = 673 K.

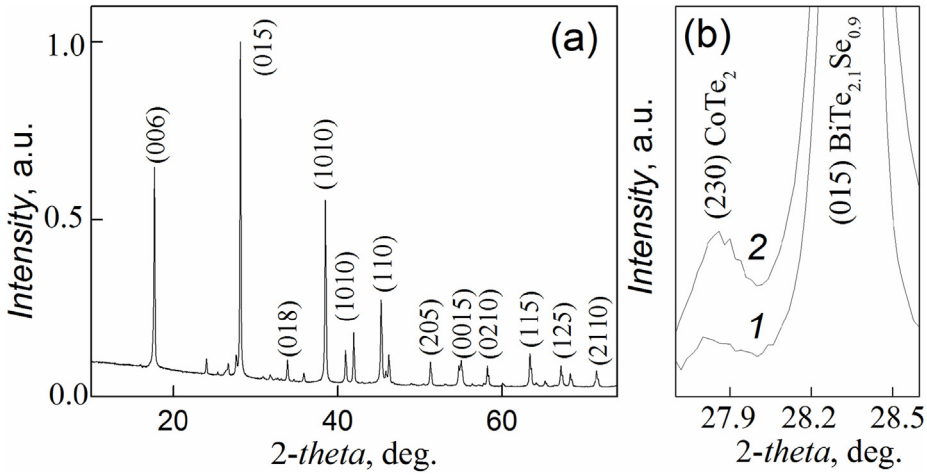

Fig. 2. (a) XRD pattern for the cermet $Bi_2Te_{2.1}Se_{0.9}$+0.33 wt% Co composite, SPS-treated at T_S = 673 K; (b) Enlarged part of XRD patterns for the composites, SPS-treated at T_S = 598 (curve *1*) and 673 K (*2*).

composite, EDS line scan profiles of Te, Bi, Se and Co were taken along line, crossing one of the inclusions. BSE image of this "core"-"shell" inclusion is shown in Fig. 4 (a). Results of EDS scanning are presented in Fig. 4 (b). One can conclude that (i) Co and Te are dominated inside the shell, (ii) Co is mainly concentrating inside the core, (iii) far from the inclusion, Co is missing, whereas Te, Bi and Se are homogenously distributed. Similarly to the Ni@$NiTe_2$ inclusions [11,12], gradient changing in Co and Te content takes place in the Co@$CoTe_2$ inclusions, too. Therefore, under SPS-treatment of the starting $Bi_2Te_{2.1}Se_{0.9}$ and Co powders, forming the local-gradient micrometer Co@$CoTe_2$ inclusions from the initial Co inclusions occurs. Besides the micrometer Co@$CoTe_2$ inclusions, nanometer inclusions with size of <100 nm are also observed in the cermet composite being studied. Some of these nanometer inclusions are highlighted by circles in Fig. 4 (a). Comparing color of the nanometer inclusions and the $CoTe_2$ shell in the Co@$CoTe_2$inclusions, one can conclude that the nanometer inclusions correspond to the $CoTe_2$ phase. As was mentioned above, the starting Co powder consists of agglomerated formations, which include many Co particles (Fig. 1 (b)). Due to chemical interaction between the $Bi_2Te_{2.1}Se_{0.9}$ matrix and the Co filler, the nanometer $CoTe_2$ inclusions could be synthesized from these initial separate Co particles, which, in turn, are formed under mixing the starting $Bi_2Te_{2.1}Se_{0.9}$ and Co powders by planetary mill. Since the separate Co particles are small, they have a time enough to totally or partially transform into the $CoTe_2$ inclusions under SPS-treatment. With increasing T_S, this transformation should be more effective, that is more number of the initial separate Co particles will transform into the final $CoTe_2$ inclusions.

The initial Co inclusions should be considered as impurity Co sources, randomly distributed inside the $Bi_2Te_{2.1}Se_{0.9}$ matrix. This initial Co distribution is strongly inhomogeneous. During SPS-treatment including both the high-temperature sintering and the uniaxial mechanical loading, the matrix and filler atoms start diffusing through matrix/filler interfaces in order to form final homogeneous Co distribution. Owing to diffusion atoms redistribution, which results in Co→$CoTe_2$ reaction, the $CoTe_2$ phase is gradually forming as the shell, surrounding the Co core. Atomic diffusion is some solid is known to be very sensitive to temperature of this process, which affects relevant diffusion coefficient [30]. In this case, with increasing T_S, more fraction of the initial Co inclusion will transform into the $CoTe_2$ shell that will be accompanied by simultaneous decreasing fraction of the Co core. As result, a ratio between fractions of the core and the shell in the Co@$CoTe_2$ inclusions should be strongly dependent on SPS-temperature. Such T_S-effect on the characteristics of the Co@$CoTe_2$ inclusions was really found. Taking into account almost spherical shape of the Co@$CoTe_2$ inclusions, average diameter of the inclusion itself, D_{IN}, and average diameter of the core, D_C, can be estimated. To correctly estimate the D_{IN} and D_C sizes, the histograms of distributions for these sizes were plotted by using BSE images, taken for different SPS-temperatures. To obtain the reliable sizes distributions, the D_c and D_{in} sizes of more than 50 inclusions were measured on BSE images. Both histograms can be satisfactory described by a lognormal unimodal distribution. The lognormal probability density function for the D_{IN} and D_C sizes can be expressed as [31].

$$F(D) = \frac{1}{\sqrt{2\pi}\sigma D}\exp\left(-\frac{(\ln D - \ln D_a)^2}{2\sigma^2}\right), \quad (1)$$

where $D = D_{IN}$ (for the histogram of D_{IN}-distribution) or $D = D_C$ (for the histogram of D_C-distribution), and σ is the standard deviation of the logarithms of the sizes.

The standard deviation of the logarithms of both sizes was estimated as ~0.4 and it was weakly dependent on sintering temperature. Then, the D_C and D_{IN} estimates were used to calculate the D_C/D_{IN} ratio that can be applied to characterize a changing in internal structure of the inclusions with varying T_S. The D_C/D_{IN} versus T_S dependence is presented in Fig. 5. With increasing T_S, the Co core fraction is gradually decreasing, i.e. the $CoTe_2$ shell is gradually becoming dominant in the Co@$CoTe_2$ inclusion. As was mentioned above, this tendency can be originated from acceleration of atomic diffusion at higher temperatures. Thus, at low SPS-

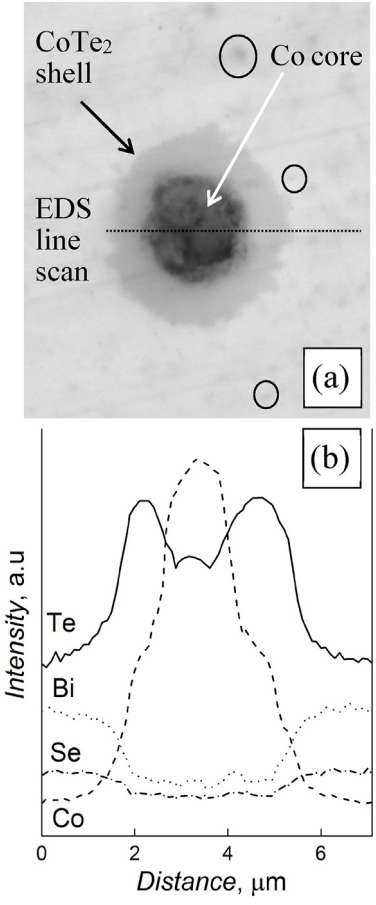

Fig. 4. (a) BSE image of the filler Co@$CoTe_2$ inclusion (circles indicate the separate $CoTe_2$ particles); (b) EDS line scan profiles of Bi, Te, Se and Co, taken along line crossing the inclusion.

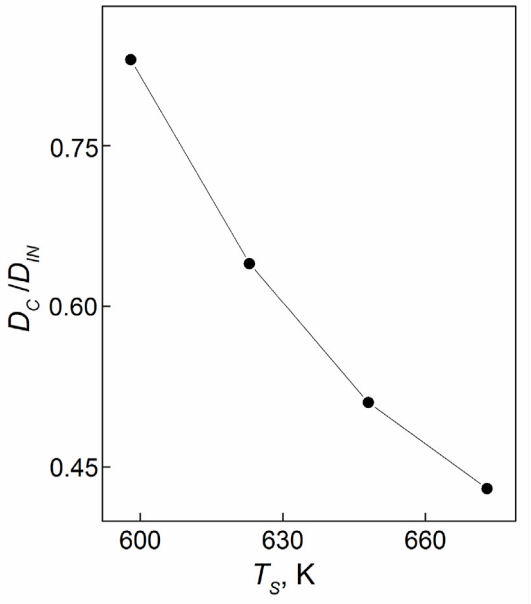

Fig. 5. The D_C/D_{IN} vs. T_S dependence for the cermet $Bi_2Te_{2.1}Se_{0.9}$+0.33 wt% Co composite.

temperatures (T_S = 598 and 623 K), the core-dominated inclusions are preferentially forming, at high SPS-temperature (673 K), the shell-dominated inclusions are main ones, and, finally, at intermediate SPS-temperature (648 K), the core and shell fractions in the inclusions are close to each other. Therefore, the internal structure of the Co@$CoTe_2$ inclusions is really governing by SPS-temperature.

All the samples of the cermet $Bi_2Te_{2.1}Se_{0.9}$+0.33 wt% Co composite SPS-treated at different T_S were found to be heavily texturing. As was mentioned above, the texturing is a typical phenomenon for Bi_2Te_3-based alloys, which are prepared by technological processes using uniaxial pressuring a starting powder [16–22,32,33]. Usually, a texturing axis coincides with SPS-pressing direction. Under the texturing, the plate-shaped grains are preferentially ordering that results in forming a specific lamellar texture. The grains are elongated along the lamellar sheets, and the sheets themselves lie in a plane, perpendicular to SPS-pressing direction. SEM-images taken for the perpendicular (perpendicularly to SPS-pressing direction) and parallel (parallel to SPS-pressing direction) surfaces of the cermet $Bi_2Te_{2.1}Se_{0.9}$+0.33 wt % Co composite SPS-treated at T_S = 598 K are presented in Fig. 6 (a) and (b), respectively. An ordered grained structure formed in the lamellar sheets is observed for the parallel surface, but a disordered grain structure with the grains having mainly irregular shape is observed for the perpendicular surface. To estimate a texturing degree of the cermet composites SPS-treated at different T_S, the Lotgering factor, *LF* was extracted via analysis of XRD patterns [34]. *LF* be expressed as

$$F = \frac{p - p_0}{1 - p_0}, \tag{2}$$

where p and p_0 are in turn expressed as

$$p = \frac{I(00l)}{\sum I(hkl)}, \text{and } p_0 = \frac{I_0(00l)}{\sum I_0(hkl)} \tag{3}$$

Here, the I and I_0 intensities correspond to textured (oriented) and non-textured (non-oriented) samples, respectively. Ideally, F = 1 corresponds to completely oriented sample (single crystal), whereas F = 0 is characteristic of completely non-oriented sample (powder or grained material with completely random grain orientation).

The *LF* versus T_S dependence is presented in Fig. 7. With increasing T_S, *LF* steady decreases. To explain this behavior, presence of the separate nanometer Co particles, which form spherical agglomerations (Fig. 1 (b)) in the starting Co powder, should be taken into account. These separate C particles can act as a lubricant during spark plasma sintering of the cermet $Bi_2Te_{2.1}Se_{0.9}$+0.33 wt% Co composites. The initial stage of SPS-process is a packing of the particles in the starting powder under external pressuring [35]. During the texturing, the packing will lead to the rearrangement of the randomly oriented particles into the lamellar sheets with preferential particles orientation. These particles will be next transformed into the grains in sintered material. Some nanometer powder lubricants can really improve the particles packing behavior during SPS-process that were reported for the Ce lubricant in Al_2O_3 [36] or the Te lubricant in Bi_2Te_3 [37]. Via the lubricating mechanism, introducing Co as separate particles should result in more effective packing the particles, and, hence, relevant increasing in preferential grain orientation. However, under SPS-treatment of the starting powders, the Co→$CoTe_2$ transformation takes place. $CoTe_2$ is chemical compound and it cannot already act as the lubricant. The Co→$CoTe_2$ transformation will be accelerated at higher temperatures. As result, with increasing T_S a fraction of lubricating Co particles will decrease, whereas a fraction non-lubricating $CoTe_2$ particles will increases. The particles packing and the following texturing will become less effective, resulting in the relevant *LF*(T_S) dependence (Fig. 7).

Synthesis of the "core"-"shell" particles of various types is already known way, applying to improve the thermoelectric properties of materials [38,39]. However, under preparation of a bulk material, an initial "core"-"shell" structure is usually destroyed [38]. In the cermet $Bi_2Te_{2.1}Se_{0.9}$+0.33 wt% Co composite, the Co@$CoTe_2$ inclusions are naturally formed inside the matrix during SPS-process. Moreover, the internal structure of the "core"-"shell" inclusions can be tuned in desired manner via varying SPS-temperature. Finally, $CoTe_2$, which is shell's material, is compound interesting for research. Particularly, at present this compound is considering as promising electrocatalyst for hydrogen evolution reaction [40–42].

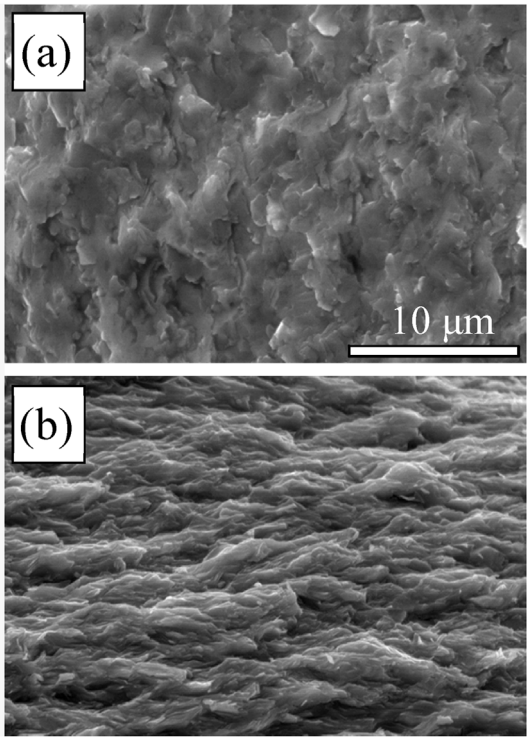

Fig. 6. SEM images for the cermet $Bi_2Te_{2.1}Se_{0.9}$+0.33 wt% Co composite with T_S = 598 K, taken for the surfaces oriented perpendicular (a) and parallel (b) to the SPS-pressing direction.

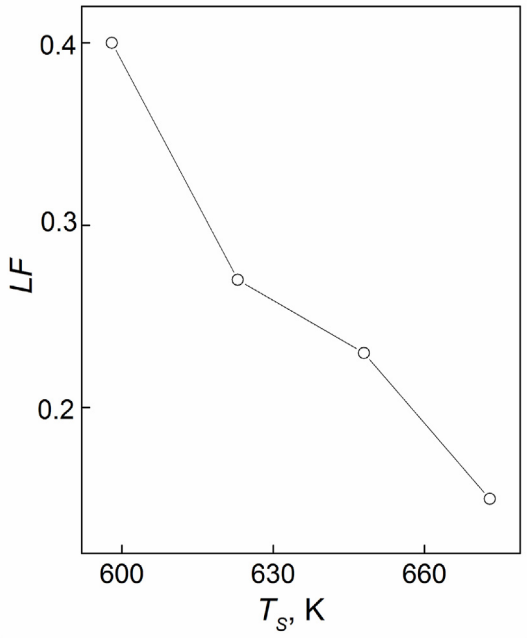

Fig. 7. The *LF* vs. T_S dependence for the cermet $Bi_2Te_{2.1}Se_{0.9}$+0.33 wt% Co composite.

All the thermoelectric properties (including the specific electrical resistance, the Seebeck coefficient and the total thermal conductivity) of the cermet $Bi_2Te_{2.1}Se_{0.9}$+0.33 wt% Co composite measured at room temperature happened to be T_S-dependent. Besides, since the composites are textured, these properties are anisotropic, too. To take into account the texturing effect, all the thermoelectric properties were measured for directions, parallel (parallel measuring orientation) and perpendicular (perpendicular measuring orientation) to SPS-pressing direction. The ρ, S and k versus T_S dependences taken for the parallel and perpendicular measuring orientations are shown in Fig. 8 (left panel). The main features in these dependences can be listed as follows. Firstly, the $\rho(T)$ curves for the perpendicular measuring orientation lie lower than the relevant $\rho(T)$ curves for the parallel measuring orientation, and the $k(T)$ curves for the perpendicular measuring orientation lie higher than the relevant $k(T)$ curves for the parallel measuring orientation. The texturing redistributes the anisotropic ρ and k contributions from crystal a-b plane (ρ_{ab} and k_{ab}) and c-axis (ρ_c and k_c) into the specific electrical resistivity and the total thermal conductivity, measured parallel (ρ_c and k_c are dominant contributions) or perpendicularly (ρ_{ab} and k_{ab} are dominant contributions) to the texturing axis [22]. Since $\rho_{ab}<\rho_c$ and $k_{ab}>k_c$, ρ increases and k decreases for the parallel measuring orientation as compared to these properties for the perpendicular measuring orientation. Secondly, usually the Seebeck coefficient is very weakly anisotropic quantity. However, in the cermet $Bi_2Te_{2.1}Se_{0.9}$+0.33 wt % Co composites, the $S(T)$ curves for the parallel measuring orientation lie higher than the relevant $S(T)$ curves for the perpendicular measuring orientation, i.e. S unexpectedly happened to be rather anisotropic. Reason of this S anisotropy is unclear now. The Seebeck coefficient has a negative sign, which is characteristic of n-type conductivity. Thirdly, with increasing T_S, the specific electrical resistivity and the Seebeck coefficient decrease,

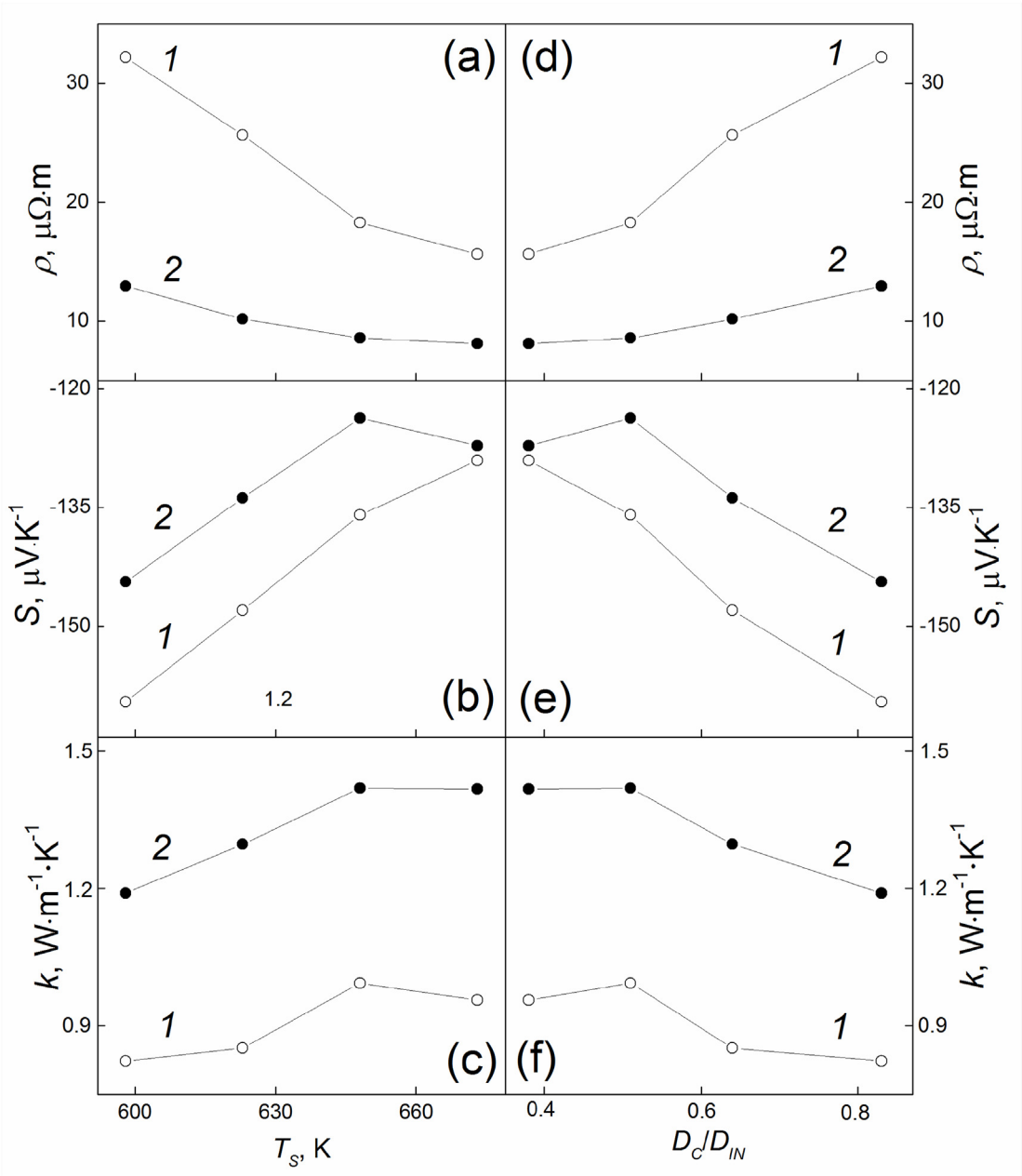

Fig. 8. Left panel: the T_S-effect on the specific electrical resistivity (a), the Seebeck coefficient (b) and the total thermal conductivity (c) of the cermet $Bi_2Te_{2.1}Se_{0.9}$+0.33 wt% Co composite, measured at room temperature for the parallel (curves *1*) and perpendicular (*2*) orientations. Right panel: the same thermoelectric properties versus the D_C/D_{IN} parameter, which characterizes the internal structure of the Co@$CoTe_2$ inclusions.

whereas the total thermal conductivity increases.

Detailed analysis of SPS-temperature on features in the microstructure and the thermoelectric properties of *n*-type grained $Bi_{1.9}Gd_{0.1}Te_3$ compound was earlier reported in Ref. [21]. In this case, the T_S-effect on the thermoelectric properties was attributed to change in the texturing degree, grains growth and forming Te-vacancies. However, in the cermet $Bi_2Te_{2.1}Se_{0.9}$+0.33 wt% Co composite, an additional mechanism of the T_S-effect on the thermoelectric properties, which is due to change in internal structure of the filler Co@$CoTe_2$ inclusions, should be taken into account. As was mentioned above, the D_C/D_{IN} ratio can be introduced to characterize the T_S-effect on the internal structure of these inclusions (Fig. 5). The thermoelectric properties shown in left panel of Fig. 8, but replotted as the D_C/D_{IN}-dependences, are presented in right panel of Fig. 8. In contrast to the T_S-dependences, with increasing D_C/D_{IN}, the specific electrical resistivity and the Seebeck coefficient increase, whereas the total thermal conductivity decreases. It is important to note that decreasing D_C/D_{IN} corresponds to reducing in fraction of the metal Col core in the filler Co@$CoTe_2$ inclusion. The D_C/D_{IN}-behavior of ρ, S and k can be attributed to increasing the electrons concentration, n, with increasing T_S. Firstly, it is known [43] that the specific electrical resistivity of the donor semiconductors can be expressed as

$$\rho = \frac{1}{e\mu n}, \tag{4}$$

where e is the charge of electron, and μ is the electron mobility.

Secondly, the Seebeck coefficient of the degenerate semiconductors can be expressed as [14].

$$S = \frac{2k_B^2 Tm^*}{3e\hbar^2}\left(\frac{\pi}{3n}\right)^{2/3}, \tag{5}$$

where m^* is the density-of-states effective mass of electrons.

Finally, it is known [43] that the lattice (or phonon) thermal conductivity and the electronic thermal conductivity are main contributions into the total thermal conductivity. The electronic thermal conductivity is related to the specific electrical resistivity through the Wiedemann-Franz law

$$k_e = \frac{L}{\rho} = Le n\mu T, \tag{6}$$

where L is a constant called as the Lorenz number.

Therefore, in accordance with expressions (4), (5) and (6), with decreasing n, the specific electrical resistivity and the Seebeck coefficient will be increasing, whereas the total thermal conductivity will be decreasing. It is known [44] that Co dopant can act as donor impurity that increases the electron concentrations in Bi_2Te_3-based compounds. Hence, in the cermet $Bi_2Te_{2.1}Se_{0.9}$+0.33 wt% Co composite, the initial Co inclusions or the Co cores can be also considered as donor sources. Under Co diffusion from these donor sources, besides forming the Co@$CoTe_2$ inclusions, the Co doping of the $Bi_2Te_{2.1}Se_{0.9}$ matrix will take place, too. This doping will result in increasing n. With increasing T_S, the fraction of the Co core reduces (Fig. 5). Then, one can conclude that the Co doping is more heavily and effective. Since this doping is related to local Co sources, it itself will be local and gradient. As result, with increasing T_S (and relevant decreasing D_C/D_{IN}), the electron concentration due to the local Co doping will be gradually increasing, affecting the thermoelectric properties in the manner that corresponds to Fig. 8.

Finally, the $\rho(T_S)$, $S(T_S)$ and $k(T_S)$ dependences measured for both orientations were used to calculate the thermoelectric figure-of-merit, ZT, of the cermet $Bi_2Te_{2.1}Se_{0.9}$+0.33 wt% Co composite (Fig. 9). The thermoelectric figure-of-merit is calculated as $ZT = TS^2/\rho k$ (T is the absolute temperature) [45]. The room temperature ZT versus T_S dependences taken for the parallel and perpendicular measuring orientations are presented by curves *1* and *2*, respectively. The ZT values are low enough and the T_S-effect on ZT is weak. For the Bi_2Te_3-based

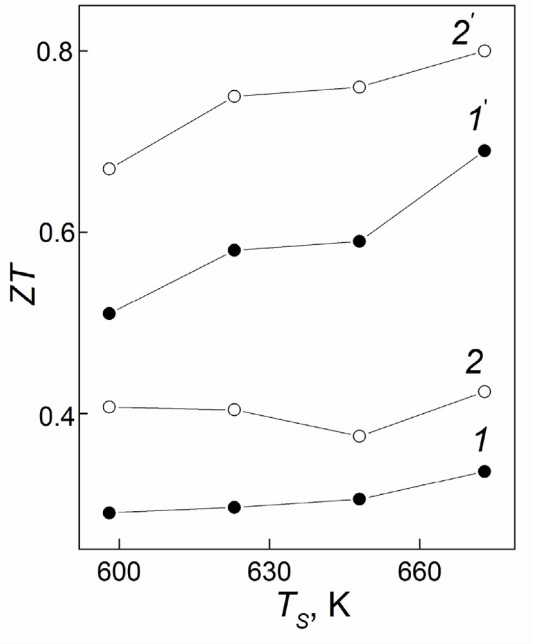

Fig. 9. The T_S-effect on the room temperature (curves *1* and *2*) and highest (*1′* and *2′*) thermoelectric figure-of-merit of the cermet $Bi_2Te_{2.1}Se_{0.9}$+0.33 wt% Co composite, measured for the parallel (*1* and *1′*) and perpendicular (*2* and *2′*) orientations.

compounds the highest ZT values are usually observed at high temperatures (450–550 K) [13,14,21]. Curves *1′* and *2′* correspond to the highest ZT_{max} values of the composite being studied measured for the parallel and perpendicular measuring orientations, respectively. The highest value of the thermoelectric figure-of-merit equal to ~0.8 is found for the perpendicular measuring orientation for the composite, SPS-treated at 673 K. It is interesting to compare the thermoelectric properties of the cermet $Bi_2Te_{2.1}Se_{0.9}$+0.33 wt% Co composite, SPS-treated at 673 K, and $Bi_2Te_{2.1}Se_{0.9}$ compound, also prepared by spark plasma sintering [23]. The $Bi_2Te_{2.1}Se_{0.9}$ compound can be considered as reference sample. The ρ, S, k and ZT values, taken at room temperature, and the highest ZT_{max} values, taken for both measuring orientations, for the cermet $Bi_2Te_{2.1}Se_{0.9}$+0.33 wt% Co composite and the reference $Bi_2Te_{2.1}Se_{0.9}$ sample are listed in Table 1.

To achieve high ZT values, an effective thermoelectric material must simultaneously have the specific electrical resistivity and the low thermal conductivity, and the high Seebeck coefficient. In accordance with data presented in Table 1, the ρ and k values of the cermet $Bi_2Te_{2.1}Se_{0.9}$+0.33 wt% Co composite are lower as compared to that for the reference $Bi_2Te_{2.1}Se_{0.9}$ sample. As result, the highest thermoelectric figure-of-merit of the cermet $Bi_2Te_{2.1}Se_{0.9}$+0.33 wt% Co composite is higher than value $ZT \approx 0.7$, reported for the $Bi_2Te_{2.1}Se_{0.9}$ compound.

Table 1
The thermoelectric properties of the cermet $Bi_2Te_{2.1}Se_{0.9}$+0.33 wt% Co composite and the reference $Bi_2Te_{2.1}Se_{0.9}$ sample.

Compound	ρ, μΩ·m	S, μV·K^{-1}	k, W·m^{-1}·K^{-1}	ZT	ZT_{max}
	per par	per par	per par	per par	per par
Cermet $Bi_2Te_{2.1}Se_{0.9}$+0.33 wt% Co composite, with T_S = 673 K	8.12 15.65	−127.2 −129.08	1.47 0.96	0.42 0.34	0.80 0.69
Reference $Bi_2Te_{2.1}Se_{0.9}$ sample [23]	10.5 27.0	−147.0 −145.0	1.51 1.12	0.46 0.27	0.68 0.37

4. Conclusion

Thus, the cermet $Bi_2Te_{2.1}Se_{0.9}$+0.33 wt % Co composite has been for the first time prepared by SPS-treatment of relevant amounts of the starting $Bi_2Te_{2.1}Se_{0.9}$ and Co powders. Effect of SPS-temperature on features in the microstructure (internal structure of the filler Co@$CoTe_2$ inclusions and the texturing degree of the grained $Bi_2Te_{2.1}Se_{0.9}$ matrix) and the thermoelectric properties was found and analyzed. Forming the "core-shell" inclusions can be applied as an additional freedom degree that will allow tuning different thermoelectric properties of the cermet composites in the desired manner.

CRediT authorship contribution statement

Marina Zhezhu: Project administration, Investigation. **Alexei Vasil'ev:** Investigation. **Maxim Yaprintsev:** Investigation. **Oleg Ivanov:** Conceptualization, Writing – review & editing. **Vseslav Novikov:** Investigation.

Declaration of competing interest

The authors declare that they have no known competing financial interests or personal relationships that could have appeared to influence the work reported in this paper.

Acknowledgements

This work was supported by the Russian Foundation for Basic Researches (grant number No 20-33-90186\20). All of studies were carried out by the scientific equipment of joint research center "Technologies and Materials" at the Belgorod State University.

References

[1] O.V. Mukbaniani, D. Balkose, H. Susanto, A.K. Haghi, Composite Materials for Industry, Electronics, and the Environment: Research and Applications, Apple Academic Press, 2000.
[2] F.C. Campbell, Structural Composite Materials, ASM International, 2010.
[3] K.K. Chawla, Composite Materials: Science and Engineering (Materials Research and Engineering), third ed., Springer, 2012.
[4] A.X. Chen, C. Yang, R.H. Wang, F. Wang, M.H. Xu, S.B. Li, J.G. Song, L. Chen, Effect of raw materials on properties of coated Al_2O_3-Al cermet materials via vacuum sintering method, Key Eng. Mater. 858 (2020) 53–58. https://doi.org/10.4028/www.scientific.net/KEM.858.53.
[5] J.F. Xu, G.Y. Liu, L. Tang, J.Y. Zhang, C. Jie, Synthesis and electrical properties of Mo-ZrO_2 cermet, Adv. Mater. Res. 311–313 (2011) 2121–2126. https://doi.org/10.4028/www.scientific.net/amr.311-313.2121.
[6] S. Ordoñez, L. Carvajal, V. Martínez, C. Agurto, J. Marín, L. Olivares, I. Iturriza, Fracture toughness of SiC-Cu based alloys cermets, Mater. Sci. Forum (2005) 498–499, 350–56, https://doi.org/10.4028/www.scientific.net/msf.498-499.350.
[7] A. Ali, A. Andriyana, Properties of multifunctional composite materials based on nanomaterials: a review, RSC Adv. 10 (2020) 16390–16403, https://doi.org/10.1039/C9RA10594H.
[8] W. Zhao, Z. Liu, P. Wei, Q. Zhang, W. Zhu, X. Su, X. Tang, J. Yang, Y. Liu, J. Shi, Y. Chao, S. Lin, Y. Pei, Magnetoelectric interaction and transport behaviours in magnetic nanocomposite thermoelectric materials, Nat. Nanotechnol. 12 (2017) 55–60, https://doi.org/10.1038/nnano.2016.182.
[9] W. Zhao, Z. Liu, Z. Sun, Q. Zhang, P. Wei, X. Mu, H. Zhou, C. Li, S. Ma, D. He, P. Ji, W. Zhu, X. Nie, X. Su, X. Tang, B. Shen, X. Dong, J. Yang, Y. Liu, J. Shi, Superparamagnetic enhancement of thermoelectric performance, Nature 13 (2017) 247–251, https://doi.org/10.1038/nature23667.
[10] R. Lu, J.S. Lopez, Y. Liu, T.P. Bailey, A.A. Page, S. Wang, C. Uher, P.F.P. Poudeu, Coherent magnetic nanoinclusions induce charge localization in half-Heusler alloys leading to high Tc ferromagnetism and enhanced thermoelectric performance, J. Mater. Chem. A. 7 (2019) 1095–11103, https://doi.org/10.1039/c9ta01156k.
[11] M. Yaprintsev, A. Vasil'ev, O. Ivanov, M. Zhezhu, E. Yaprintseva, V. Novikov, Enhanced thermoelectric efficiency of the bulk composites consisting of "Bi_2Te_3 matrix" and "filler Ni@$NiTe_2$ inclusions, Scripta Mater. 194 (2021), https://doi.org/10.1016/j.scriptamat.2020.113710, 113710-113711-4.
[12] M. Yaprintsev, A. Vasil'ev, O. Ivanov, M. Zhezhu, E. Yaprintseva, V. Novikov, Forming the locally-gradient Ni@$NiTe_2$ domains from initial Ni inclusions embedded into thermoelectric Bi_2Te_3 matrix, Mater. Lett. 290 (2021), https://doi.org/10.1016/j.matlet.2021.129451, 129451-1-4.
[13] H.J. Goldsmid, Bismuth telluride and its alloys as materials for thermoelectric generation, Mater 7 (2014) 2577–2592, https://doi.org/10.3390/ma7042577.
[14] H. Scherrer, S. Scherrer, Thermoelectrics Handbook: Macro to Nano, CRC Taylor and Francis, Boca Raton, 2012.
[15] B.D. Cullity, C.D. Graham, Introduction to Magnetic Materials, IEEE Press, Piscataway, 2009.
[16] S.D. Bhame, D. Pravarthana, W. Prellier, J.G. Noudem, Enhanced thermoelectric performance in spark plasma textured bulk *n*-type $Bi_2Te_{2.7}Se_{0.3}$ and *p*-type $Bi_{0.5}Sb_{1.5}Te_3$, Appl. Phys. Lett. 102 (2013), https://doi.org/10.1063/1.4813262, 2190-2191-3.
[17] X.A. Fan, J.Y. Yang, R.G. Chen, H.S. Yun, W. Zhu, S.Q. Bao, X.K. Duan, Characterization and thermoelectric properties of *p*-type 25%Bi_2Te_3–75%Sb_2Te_3 prepared via mechanical alloying and plasma activated sintering, J. Phys. D Appl. Phys. 39 (2006) 740–745, https://doi.org/10.1088/0022-3727/39/4/021.
[18] J. Jiang, L. Chen, S. Bai, Q. Yao, Q. Wang, Fabrication and thermoelectric performance of textured *n*-type $Bi_2(Te, Se)_3$ by spark plasma sintering, Mater. Sci. Eng. B 117 (2005) 334–338, https://doi.org/10.1016/j.mseb.2005.01.002.
[19] Q. Lognon, F. Gascoin, O.I. Lebedev, L. Lutterotti, S. Gascoin, D. Chateigner, Quantitative texture analysis of spark plasma textured *n*-Bi_2Te_3, J. Am. Ceram. Soc. 97 (2014) 2038–2045, https://doi.org/10.1111/jace.12970.
[20] A. Vasil'ev, M. Yaprintsev, O. Ivanov, E. Danshina, Anisotropic thermoelectric properties of $Bi_{1.9}Lu_{0.1}Te_{2.7}Se_{0.3}$ textured via spark plasma sintering, Solid State Sci. 84 (2018) 28–430, https://doi.org/10.1016/j.solidstatesciences.2018.08.004.
[21] M. Yaprintsev, A. Vasil'ev, O. Ivanov, Thermoelectric properties of the textured $Bi_{1.9}Gd_{0.1}Te_3$ compounds spark-plasma-sintered at various temperatures, J. Eur. Ceram. Soc. 40 (2019) 742–750, https://doi.org/10.1016/j.jeurceramsoc.2019.11.028.
[22] O. Ivanov, M. Yaprintsev, A. Vasil'ev, Comparative analysis of the thermoelectric properties of the non-textured and textured $Bi_{1.9}Gd_{0.1}Te_3$ compounds, J. Solid State Chem. 290 (2020), https://doi.org/10.1016/j.jssc.2020.121559, 121559-1-10.
[23] D. Li, X.Y. Qin, J. Zhang, C.J. Song, Y.F. Liu, L. Wang, H.X. Xin, Z.M. Wang, Thermoelectric anisotropy of *n*-type $Bi_2Te_{3-x}Se_x$ prepared by spark plasma sintering, RSC Adv. (2015) 43717–43722, https://doi.org/10.1039/c5ra04435a.
[24] B. Hamawandi, S. Ballikaya, H. Batili, V. Roosmark, M. Orlovská, A. Yusuf, M. Johnsson, R. Szukiewicz, M. Kuchowicz, M.S. Toprak, Facile solution synthesis, processing and characterization of *n*- and *p*-type binary and ternary Bi–Sb tellurides, Appl. Sci. 10 (2020), https://doi.org/10.3390/app10031178, 1178-1-13.
[25] D. Li, X.Y. Qin, Y.F. Liu, N.N. Wang, C.J. Song, R.R. Sun, Improved thermoelectric properties for solution grown $Bi_2Te_{3-x}Se_x$ nanoplatelet composites, RSC Adv. 3 (2013) 2632–2638, https://doi.org/10.1039/c2ra22562j.
[26] M. Loor, G. Bendt, U. Hagemann, C. Wölper, W. Assenmacher, S. Schulz, Synthesis of Bi_2Te_3 and $(Bi_xSb_{1-x})_2Te_3$ nanoparticles using the novel IL [C4mim]3[Bi3I12], Dalton Trans. 45 (2016) 15326–15335, https://doi.org/10.1039/c6dt02361d.
[27] X.B. Zhao, X.H. Ji, Y.H. Zhang, G.S. Cao, J.P. Tu, Hydrothermal synthesis and microstructure investigation of nanostructured bismuth telluride powder, Appl. Phys. A 80 (2005) 1567–1571, https://doi.org/10.1007/s00339-004-2956-8.
[28] J.R. Drabble, C.H.L. Goodman, Chemical bonding in bismuth telluride, J. Phys. Chem. Solid. 5 (1958) 142–144, https://doi.org/10.1016/0022-3697(58)90139-2.
[29] S. Nakajima, The crystal structure of $Bi_2Te_{3-x}Se_x$, J. Phys. Chem. Solid. 24 (1963) 479–485. https://doiorg/10.1016/0022-3697(63)90207-5.
[30] H. Mehrer, Diffusion in Solids. Fundamentals, Methods, Materials, Diffusion-Controlled Processes, Springer-Verlag Berlin Heidelberg, 2007.
[31] F.J. Humphreys, M. Hatherly, Recrystallization and Related Annealing Phenomena, Elsevier, Oxford, UK, 2004.
[32] S.S. Kim, S. Yamamoto, T. Aizawa, Thermoelectric properties of anisotropy-controlled *p*-type Bi-Te-Sb system via bulk mechanical alloying and shear extrusion, J. Alloys Compd. 375 (2004) 107–113, https://doi.org/10.1016/j.jallcom.2003.11.141.
[33] Y. Morisaki, H. Araki, H. Kitagawa, M. Orihashi, K. Hasezaki, K. Kimura, Bi_2Te_3-related thermoelectric samples with aligned-texture prepared by plastic deformation, Mater. Trans. 46 (2005) 2518–2524, https://doi.org/10.2320/matertrans.46.2518, 2518.
[34] F.K. Lotgering, Topotactical reactions with ferrimagnetic oxides having hexagonal crystal structures—I, J. Inorg. Nucl. Chem. 9 (1959) 113–123, https://doi.org/10.1016/0022-1902(59)80070-1.
[35] L. Wang, V. Pouchly, K. Maca, Z. Shen, Y. Xiong, Intensive particle rearrangement in the early stage of spark plasma sintering process, J. Asian Ceram. Soc. 3 (2015) 183–187, https://doi.org/10.1016/j.jascer.2015.02.004.
[36] I. Alvarez-Clemares, G. Mata-Osoro, A. Fernandez, S. Lopez-Esteban, C. Pecharroman, J. Palomares, R. Torrecillas, J. Serafín Moya, Transparent alumina/ceria nanocomposites by spark plasma sintering, Adv. Eng. Mater. 12 (2010) 1154–1160. https://doi.org/10.1002/adem.201000176.
[37] Y. Liu, Y. Zhang, K.H. Lim, M. Ibanez, S. Ortega, M. Li, J. David, S. Martí-Sánchez, K.M. Ng, J. Arbiol, M.V. Kovalenko, D. Cadavid, A. Cabot, High thermoelectric performance in crystallographically textured *n*-type $Bi_2Te_{3-x}Se_x$ produced from asymmetric colloidal nanocrystals, ACS Nano 12 (2018) 7174–7184, https://doi.org/10.1021/acsnano.8b03099.
[38] O. Ivanov, O. Maradudina, R. Lyubushkin, Preparation and characterization of bulk composite constructed of Bi_2Te_3@SiO_2 nanoparticles, J. Alloys Compd. 586 (2014) 679–682, https://doi.org/10.1016/J.JALLCOM.2013.10.090.
[39] J.-H. Bahk, P. Santhanam, Z. Bian, R. Ram, A. Shakouri, Resonant carrier scattering by core-shell nanoparticles for thermoelectric power factor enhancement, Appl. Phys. Lett. 100 (2012), https://doi.org/10.1063/1.3673615, 012102-1-4.
[40] T.-H. Lu, C.-J. Chen, M. Basu, C.-G. Ma, R.-S. Liu, The $CoTe_2$ nanostructure: an efficient and robust catalyst for hydrogen evolution, Chem. Commun. 51 (2015) 17012–17015, https://doi.org/10.1039/c5cc06806a.
[41] Y. Qi, J. Wu, J. Xu, H. Gao, Z. Du, B. Liu, L. Liu, D. Xiong, One-step fabrication of a self-supported Co@$CoTe_2$ electrocatalyst for efficient and durable oxygen evolution

reactions, Inorg. Chem. Front. 7 (2020) 2523–2532, https://doi.org/10.1039/d0qi00372g.
[42] X. Chia, Z. Sofer, J. Luxa, M. Pumera, Unconventionally layered $CoTe_2$ and $NiTe_2$ as electrocatalysts for hydrogen evolution, Chem. A. European J. 23 (2017) 11719–11726, https://doi.org/10.1002/chem.201702753.
[43] J.S. Blakemore, Solid State Physics, Cambridge University Press, Cambridge, 1985.
[44] K.C. Lukas, W.C. Liu, Z.F. Ren, C.P. Opeil, Transport properties of Ni, Co, Fe, Mn doped $Cu_{0.01}Bi_2Te_{2.7}Se_{0.3}$ for thermoelectric device applications, J. Appl. Phys. 112 (2012), https://doi.org/10.1063/1.4749806, 054509-1-5.
[45] G.J. Snyder, Figure of merit *ZT* of a thermoelectric device defined from materials properties, Energy Environ. Sci. 10 (2017) 2280–2283, https://doi.org/10.1039/c7ee02007d.